PHILOSOPHICAL TRANSACTIONS A

rsta.royalsocietypublishing.org

Research

Article submitted to journal

Subject Areas:
Image processing, Computer vision, Electromagnetism

Keywords:
Inductive thermal video, tensor decomposition, hierarchical sparse, defect defection.

Author for correspondence:
Bin Gao
e-mail: bin_gao@uestc.edu.cn

Hierarchical Low Rank and Sparse Tensor Micro Defects Decomposition By Electromagnetic Thermography Imaging System

Tongle Wu[1], Bin Gao[*] and Wai lok Woo[2]

[1,*]Department of Automation Engineering, University of Electronic Science and technology
[2]Department of Computer and Information Sciences, Northumbria University

With the advancement of electromagnetic induction thermography and imaging technology in non-destructive testing field, this system has significantly benefitted modern industries in fast and contactless defects detection. However, due to the limitations of front-end hardware experimental equipment and the complicated test pieces, these have brought forth new challenges to the detection process. Making use of the spatio-temporal video data captured by the thermal imaging device and linking it with advanced video processing algorithm to defects detection becomes a necessary alternative way to solve these detection challenges. The extremely weak and sparse defect signal is buried in complex background with the presence of strong noise in the real experimental scene has prevented progress to be made in defects detection. In this paper, we propose a novel hierarchical low rank and sparse tensor decomposition (HLSTD) method to mine anomalous patterns in the induction thermography stream for defects detection. The proposed algorithm offers advantages not only in suppressing the interference of strong background and sharpens the visual features of defects, but also overcoming the problems of over- and under-sparseness suffered by similar state-of-the-art algorithms. Real-time natural defect detection experiments have been conducted to verify that the proposed algorithm is more efficient and accurate than existing algorithms in terms of visual presentations and evaluation criteria.

THE ROYAL SOCIETY PUBLISHING

1. Introduction

Non-Destructive Testing (NDT) is an indispensable and effective tool for industrial development. To some extent, it reflects the level of industrial development of a country. The importance of NDT has been recognized in recent years. These mainly include Radiographic Testing(RT) [1], Ultrasonic Testing(UT) [2], Magnetic Particle Testing(MPT) [3] and Liquid Penetrate Testing(LPT) [4]. Comparing with traditional methods, Inducing Heating (IT) focuses the heat on the defect due to friction or eddy current distortion, which increases the temperature contrast between the defective and defect-free regions. Thermal pattern contrast [5] is a relatively novel NDT method which has the advantages of fast, non-contact, non-interaction and provides full field visual information.

Non-destructive testing technology of IT integrated thermal image diagnosis system has been urgently demanded in the manufacturing industry and railway domain. Bai et al.[6] proposed a method to separate anomalous patterns from the transient thermal pattern by applying IT. Cheng et al. [7] applied the IT to detect and separate the impact damage. Genest [8] used the IT to detect the crack defects. Netzelmann [9] utilized the IT to study the external influence of the magnetic field for the thermal contrast of crack type defects. He et al. applied IT for evaluating impact in CFRP laminates and detection corrosion blister [10].

Considering that the defect size is distributed in a sparse way within the whole specimen, from imaging viewpoint this corresponds to an image with anomalous thermal pattern embedded in the background of normal thermal pattern spanned with low rank property. In this situation, the sparse and low rank-based learning methods have become very useful tools as post-processing algorithms. In order to overcome the sensitivity of the commonly used Principal Component Analysis (PCA) methods to abnormal outliers, the low rank background and sparse foreground separation algorithm based on Robust PCA (RPCA) [29] has been proposed. Some related references can be found in [30-32]. In addition, some other RPCA-based variants have emerged which include Variational RPCA [11], Non-convex RPCA [12], Online RPCA [13]. Gao et.al [14] proposed a sparse nonnegative matrix decomposition under variational Bayesian framework to extract defect features. To avoid tuning model parameters, Gao et.al [15] proposed a variational Bayesian approach to extract sub-group of sparse components e for diagnostic imaging. Wang et al.[16] proposed a thermal pattern-based contrast enhancing algorithm based on sparse abnormal optical flow field. Nevertheless, the aforementioned algorithms require the reshaping of raw three-dimensional stream of video data into a two-dimensional matrix form, which can destroy the essential structure spatial-temporal information [17]. In other way, the papers in [33-36] attempted to investigate the adaptation of structured norms to avoid destroying the essential structure of the spatial-temporal information under certain circumstances in the matrix-wise decomposition. Concretely, these alternating methods use the low rank matrix and structured sparseness to model the spatial-temporal information in the dataset.

Instead of vector or matrix representation, a higher-order tensor represented as a multidimensional array provides a more faithful representation of the intrinsic structure underlying such data ensembles. In the machine learning field, CANDECOMP/PARAFAC and Tucker factorizations [18] are prominent baseline algorithms used in the tensor decomposition approach. For the same aim to reduce the sensibility to sparse outlies, Zhao et al. [19] presented the Bayesian robust tensor factorization (BRTF) algorithm for incomplete tensor data. The method provides good results on background subtraction and object recognition such as human faces. Zhou et al.[20] proposed an Outlier-Robust Tensor PCA(OR-TPCA) for simultaneous low-rank tensor recovery and outlier detection. Lu et.al proposed TRPCA [17] based on t-SVD with new tensor nuclear norm. Recently, based on the excellent performance of nonconvex model, Xu et al.[37] Proposed nonconvex rank minimization to extract low rank tensor. Chen et al.[38] used non-convex empirical Bayes method to model low rank tensor. In addition, based on the application in flow data, stochastic[39], incremental tensor[40] and recursive[41] tensor decomposition algorithms have also been proposed. In the field of NDT applications,

Gao et.al [21] utilized the CP decomposition to model thermography spatial-transient-stage and material property characterization. Gao et.al [22] proposed multidimensional tensor-based inductive thermography to detect offshore wind turbine gear inspection. In order to fully mine spatio-temporal video information, Lu et.al [23] proposed ensemble variational Bayesian tensor factorization for super resolution of CFRP debond detection.

Comparing with many emerging tensor-based algorithms in the field of machine learning, they are less widely applied in the field of NDT. In NDT, the surface morphology of the tested specimen is different, the defect is extremely tiny and irregular. Thus, it is difficult to capture the characteristics of the defect due to the complex background and strong noise. These factors render the existing tensor machine learning algorithms handicapped when applied to defect detection. These algorithms cannot accurately separate the defects from the background and noise when the sparseness characteristics of the defects failed to be estimated correctly. This yields erroneous interpretation of the defects whether these defects are attributed to a single profile or multiple profiles of sparse components. In this paper, we propose a novel hierarchical low rank and sparse tensor decomposition(HLSTD) algorithm. This makes full exploitation of the sparse and low rank component by robust factorization for core tensor. The separated foreground information with sparse outliers is embedded in the background of low rank coefficient representations. Contributions of this article are listed below.

1) Under the proposed tensor factorization framework, the weak and small size sparse defects can be effectively extracted from the intense complex thermal patterns. The visual contrast with the surrounding normal background is significantly improved along with the well preserved background information. This helps the users or the automated diagnostic system to evaluate the presence of defects and to determine the optimal sparseness in order to obtain a faithful representation of the video data factorization.
2) Development of Augmented Lagrangian Alternative Direction Minimization (AL-ADM) [24] numerical method to optimize the parameters of the proposed model. This enables efficient implementation of the proposed algorithm for effective detection task.

The rest of this paper has been organized as follows: the proposed algorithm is described in Section 2. The experimental setup and introduction of the specimens are given in Section 3. Analysis of results are elaborated in Section 4. Finally, conclusions are drawn in Section 5.

2. Methodlogy

(a) Proposed Model

The electromagnetic thermal image sequence can be modeled as a three-dimensional tensor structure $\boldsymbol{\mathcal{D}} \in \mathbb{R}^{W \times H \times T}$. where W and H denote the resolution of image length and width, respectively. T denotes the number of frames in whole thermal video. Under the existing low rank and sparse tensor decomposition frameworks, the mathematical model is expressed as follows:

$$\begin{aligned} &\min_{\boldsymbol{\mathcal{L}},\boldsymbol{\mathcal{E}}} \|\boldsymbol{\mathcal{L}}\|_* + \lambda\|\boldsymbol{\mathcal{E}}\|_1 \\ &\text{s.t.} \quad \boldsymbol{\mathcal{D}} = \boldsymbol{\mathcal{L}} + \boldsymbol{\mathcal{E}} \end{aligned} \tag{2.1}$$

where $\|\|_*$ and $\|\|_1$ can be regarded as low rank and sparse constraints to extract the low rank tensor L and the sparse tensor E, respectively. In the field of NDT applications, the image of defects is embedded in the background of the specimen in the form of sparse distribution. The aim is to extract the sparse defect thermal pattern $\boldsymbol{\mathcal{E}}$ by using the decomposition model. However, this kind of direct decomposition model is affected by the parameters λ, resulting in either under-sparse or over-sparse detection results. Therefore, by integrating the above robust decomposition methods, we propose the following Hierarchical Low Rank Sparse Tensor Decomposition based on HOSVD [18].

$$\begin{aligned}
&\min_{\mathcal{L},\mathcal{G},\mathcal{W},\mathcal{E},\boldsymbol{U}^{(1)},\boldsymbol{U}^{(2)},\boldsymbol{U}^{(3)}} \|\mathcal{G}\|_* + \lambda\|\mathcal{W}\|_1 + \|\mathcal{E}\|_1 \\
&\text{s.t.} \quad \mathcal{D} = \mathcal{L} \times_1 \boldsymbol{U}^{(1)} \times_2 \boldsymbol{U}^{(2)} \times_3 \boldsymbol{U}^{(3)} + \mathcal{E} \\
&\qquad \mathcal{L} = \mathcal{G} + \mathcal{W} \\
&\qquad {\boldsymbol{U}^{(1)}}^T \boldsymbol{U}^{(1)} = \boldsymbol{I} \\
&\qquad {\boldsymbol{U}^{(2)}}^T \boldsymbol{U}^{(2)} = \boldsymbol{I} \\
&\qquad {\boldsymbol{U}^{(3)}}^T \boldsymbol{U}^{(3)} = \boldsymbol{I}
\end{aligned} \tag{2.2}$$

Comparing with the state-of the art RTPCA models such as (2.1), it separates the sparse defection thermal pattern into component $\mathcal{E}$ by default. Nevertheless, if λ is set too large it will result in over-sparseness in $\mathcal{E}$, which means that only high heat thermal mode is extracted without background reference. If λ is set too small, it will result in under-sparseness which subsequently causes a considerable amount of thermal pattern artifacts (or interference) remaining in $\mathcal{E}$. According to [17] advice for setting $\lambda = \frac{1}{\sqrt{T\max(W,H)}}$, existing algorithms always get over-sparse results. Proposed method utilize $\mathcal{G} \times_1 \boldsymbol{U}^{(1)} \times_2 \boldsymbol{U}^{(2)} \times_3 \boldsymbol{U}^{(3)} + \mathcal{E}$ as a final result of defect detection. $\mathcal{W} \times_1 \boldsymbol{U}^{(1)} \times_2 \boldsymbol{U}^{(2)} \times_3 \boldsymbol{U}^{(3)}$ denotes background of supplementary certification defect detection or weak tiny defection signal. $\mathcal{G} \times_1 \boldsymbol{U}^{(1)} \times_2 \boldsymbol{U}^{(2)} \times_3 \boldsymbol{U}^{(3)}$ denotes complex and high thermal interference caused by strong noise and specimen characteristics. Hyperparameter we need to tune in our algorithm is the mode of core tensor, r_1, r_2, r_3,$\mathbf{L} \in \mathbb{R}^{r_1 \times r_2 \times r_3}$. Combined setting λ as $\frac{1}{\sqrt{r_3 \max(r_1,r_2)}}$ with the additive representation of two tensors for the final result, proposed method could robustly extract tiny and weak defection image signal.

(b) Optimization Steps

In this paper, we will use the Augmented Lagrangian Alternating Direction Minimization (AL-ADM) for tuning the model parameters. T-SVD based new tensor nuclear norm $\|\|_*$ as a low rank constraint could better capture the global spatio-temporal information [17]. Thus, we adopt a similar tensor nuclear norm for the formulation of the proposed model. Reformulating the constraint optimization problem (2) into unconstraint formulation by AL-ADM, this gives the following:

$$\begin{aligned}
&L_\rho(\mathcal{L},\mathcal{G},\mathcal{W},\mathcal{E},\boldsymbol{U}^{(1)},\boldsymbol{U}^{(2)},\boldsymbol{U}^{(3)};\boldsymbol{\lambda}_1,\boldsymbol{\lambda}_2) = \|\mathcal{G}\|_* + \lambda\|\mathcal{W}\|_1 \\
&+ \|\mathcal{E}\|_1 + \boldsymbol{\lambda}_1(\mathcal{D} - \mathcal{L} \times_1 \boldsymbol{U}^{(1)} \times_2 \boldsymbol{U}^{(2)} \times_3 \boldsymbol{U}^{(3)} - \mathcal{E}) + \boldsymbol{\lambda}_2(\mathcal{L} \\
&- \mathcal{G} - \mathcal{W}) + \frac{\rho}{2}[\|\mathcal{D} - \mathcal{L} \times_1 \boldsymbol{U}^{(1)} \times_2 \boldsymbol{U}^{(2)} \times_3 \boldsymbol{U}^{(3)} - \mathcal{E}\|^2 \\
&+ \|\mathcal{L} - \mathcal{G} - \mathcal{W}\|^2]
\end{aligned} \tag{2.3}$$

Under the proximal operator and SVD decomposition, the above decouple variables are solved by the alternating minimization method which yields a closed-form solution. The solution to (3) is obtained using the following steps:

(1) Update $\boldsymbol{U}^{(i)}$, for $i = 1, 2, 3$ Extract items related to $\boldsymbol{U}^{(i)}$, we just need to minimize the following

formula:

$$\begin{aligned}\boldsymbol{U}^{(i)} &= \underset{\boldsymbol{U}^{(i)^T}\boldsymbol{U}^{(i)}=\boldsymbol{I}}{arg\min}\ \boldsymbol{\lambda}_1(\boldsymbol{\mathcal{D}}-\boldsymbol{\mathcal{L}}\times_1\boldsymbol{U}^{(1)}\times_2\boldsymbol{U}^{(2)}\times_3\boldsymbol{U}^{(3)}-\boldsymbol{\mathcal{E}}) \\ &+\frac{\rho}{2}\|\boldsymbol{\mathcal{D}}-\boldsymbol{\mathcal{L}}\times_1\boldsymbol{U}^{(1)}\times_2\boldsymbol{U}^{(2)}\times_3\boldsymbol{U}^{(3)}-\boldsymbol{\mathcal{E}}\|^2 \\ &= \underset{\boldsymbol{U}^{(i)^T}\boldsymbol{U}^{(i)}=\boldsymbol{I}}{arg\min}\ \frac{\rho}{2}\|\boldsymbol{\mathcal{D}}-\boldsymbol{\mathcal{L}}\times_1\boldsymbol{U}^{(1)}\times_2\boldsymbol{U}^{(2)}\times_3\boldsymbol{U}^{(3)}-\boldsymbol{\mathcal{E}}+\frac{\boldsymbol{\lambda}_1}{\rho}\|^2\end{aligned} \tag{2.4}$$

Because $\boldsymbol{U}^{(1)}$, $\boldsymbol{U}^{(2)}$, $\boldsymbol{U}^{(3)}$ have similar variable status. Here we only deduce the optimization steps in detail for $\boldsymbol{U}^{(1)}$, and $\boldsymbol{U}^{(2)}$ and $\boldsymbol{U}^{(3)}$ can be analogized.

$$\begin{aligned}\boldsymbol{U}^{(1)} &= \underset{\boldsymbol{U}^{(1)^T}\boldsymbol{U}^{(1)}=\boldsymbol{I}}{arg\min}\ \|\boldsymbol{D}_{<1>}-\boldsymbol{U}^{(1)}\boldsymbol{L}_{<1>}[\boldsymbol{U}^{(3)}\bigotimes\boldsymbol{U}^{(2)}]^T- \\ &(\boldsymbol{E}-\frac{\boldsymbol{\lambda}_1}{\rho})_{<1>}\|^2 = \underset{\boldsymbol{U}^{(1)^T}\boldsymbol{U}^{(1)}=\boldsymbol{I}}{arg\max}\ Tr[\boldsymbol{U}^{(1)^T}(\boldsymbol{D}-\boldsymbol{E}+\frac{\boldsymbol{\lambda}_1}{\rho})_{<1>} \\ &\boldsymbol{U}^{(3)}\bigotimes\boldsymbol{U}^{(2)}\boldsymbol{L}_{<1>}^T]\end{aligned} \tag{2.5}$$

Let $P=(\boldsymbol{D}-\boldsymbol{E}+\frac{\boldsymbol{\lambda}_1}{\rho})_{<1>}\boldsymbol{U}^{(3)}\bigotimes\boldsymbol{U}^{(2)}\boldsymbol{L}_{<1>}^T$ and $[\boldsymbol{U}_P,\boldsymbol{S}_P,\boldsymbol{V}_P]=SVD(P)$. From the solution of well-known Orthogonal Procrustes problem [26]:

$$\boldsymbol{U}^{(1)}=\boldsymbol{U}_{P(1:r_1)}\boldsymbol{V}_{P(1:r_1)}^T \tag{2.6}$$

Similarly, the solution of

$$\boldsymbol{U}^{(2)},\boldsymbol{U}^{(3)}$$

can be obtained as follows:

$$\begin{aligned}P&=(\boldsymbol{D}-\boldsymbol{E}+\frac{\boldsymbol{\lambda}_1}{\rho})_{<2>}\boldsymbol{U}^{(3)}\bigotimes\boldsymbol{U}^{(1)}\boldsymbol{L}_{<2>}^T \\ \boldsymbol{U}^{(2)}&=\boldsymbol{U}_{P(1:r_2)}\boldsymbol{V}_{P(1:r_2)}^T \\ P&=(\boldsymbol{D}-\boldsymbol{E}+\frac{\boldsymbol{\lambda}_1}{\rho})_{<3>}\boldsymbol{U}^{(2)}\bigotimes\boldsymbol{U}^{(1)}\boldsymbol{L}_{<3>}^T \\ \boldsymbol{U}^{(3)}&=\boldsymbol{U}_{P(1:r_3)}\boldsymbol{V}_{P(1:r_3)}^T\end{aligned} \tag{2.7}$$

(2) Update $\boldsymbol{\mathcal{G}}$

$$\boldsymbol{\mathcal{G}}=arg\min\ \|\boldsymbol{\mathcal{G}}\|_*+\frac{\rho}{2}\|\boldsymbol{\mathcal{L}}-\boldsymbol{\mathcal{G}}-\boldsymbol{\mathcal{W}}+\frac{\boldsymbol{\lambda}_2}{\rho}\|^2 \tag{2.8}$$

A above minimization problem is to compute the proximal operator of TNN [17]. It can be sloved by tensor Sigular Value Thresholding (t-SVT) operators which is extension of matrix SVT and has closed-form solution. Based on T-SVD, Algorithm 1 give efficient T-SVT computing method. Now

$$\boldsymbol{\mathcal{G}}=t-SVD(\boldsymbol{\mathcal{L}}-\boldsymbol{\mathcal{W}}+\frac{\boldsymbol{\lambda}_2}{\rho},\frac{1}{\rho}) \tag{2.9}$$

(3) Update $\boldsymbol{\mathcal{W}}$

$$\boldsymbol{\mathcal{W}}=arg\min\ \lambda\|\boldsymbol{\mathcal{W}}\|_1+\frac{\rho}{2}\|\boldsymbol{\mathcal{L}}-\boldsymbol{\mathcal{G}}-\boldsymbol{\mathcal{W}}+\frac{\boldsymbol{\lambda}_2}{\rho}\|^2 \tag{2.10}$$

From well-known Soft-Thresholding algorithm

$$\boldsymbol{\mathcal{W}}=S_{\frac{\lambda}{\rho}}(\boldsymbol{\mathcal{L}}-\boldsymbol{\mathcal{G}}+\frac{\boldsymbol{\lambda}_2}{\rho}) \tag{2.11}$$

where $S_{\frac{\lambda}{\rho}}(X)=sgn(X)[|X|-\frac{\lambda}{\rho}]_+$

Algorithm 1 Tensor Singular Value Thresholding:t-SVT($\boldsymbol{\mathcal{Y}}, \tau$)

Input: $\boldsymbol{\mathcal{Y}} \in \mathbb{R}^{l_1 \times l_2 \times N}$; constant $\tau > 0$;
Output: $\boldsymbol{\mathcal{X}}$
$\overline{\boldsymbol{\mathcal{Y}}} = fft(\boldsymbol{\mathcal{Y}}, [\,], 3)$.
Perform matrix SVT on each frontal slice of $\overline{\boldsymbol{\mathcal{Y}}}$ by
for $i = 1, \cdots, \lceil \frac{N+1}{2} \rceil$ **do**
$[\boldsymbol{U}, \boldsymbol{S}, \boldsymbol{V}] = SVD(\overline{\boldsymbol{Y}}^{(i)})$;
$\overline{\boldsymbol{X}}^{(i)} = \boldsymbol{U}(\boldsymbol{S} - \tau)_+ \boldsymbol{V}^*$;
end for
for $i = \lceil \frac{N+1}{2} \rceil + 1, \cdots, N$ **do**
$\overline{\boldsymbol{X}}^{(i)} = [\overline{\boldsymbol{X}}^{(N-i+2)}]^*$;
end for
$\boldsymbol{\mathcal{X}} = ifft(\overline{\boldsymbol{\mathcal{X}}}, [\,], 3)$

(4) Update $\boldsymbol{\mathcal{L}}$

$$\begin{aligned} \boldsymbol{\mathcal{L}} = arg\min\ & \frac{\rho}{2}[\|\boldsymbol{\mathcal{D}} - \boldsymbol{\mathcal{L}} \times_1 \boldsymbol{U}^{(1)} \times_2 \boldsymbol{U}^{(2)} \times_3 \boldsymbol{U}^{(3)} - \boldsymbol{\mathcal{E}} \\ & + \frac{\boldsymbol{\lambda}_1}{\rho}\|^2 + \|\boldsymbol{\mathcal{L}} - \boldsymbol{\mathcal{G}} - \boldsymbol{\mathcal{W}} + \frac{\boldsymbol{\lambda}_2}{\rho}\|^2] \end{aligned} \tag{2.12}$$

Above is a smooth convex optimization problem, thus we can obtain a closed-form solution:

$$\boldsymbol{\mathcal{L}} = \frac{(\boldsymbol{\mathcal{D}} - \boldsymbol{\mathcal{E}} + \frac{\boldsymbol{\lambda}_1}{\rho}) \times_1 \boldsymbol{U}^{(1)} \times_2 \boldsymbol{U}^{(2)} \times_3 \boldsymbol{U}^{(3)} + \boldsymbol{\mathcal{G}} + \boldsymbol{\mathcal{W}} - \frac{\boldsymbol{\lambda}_2}{\rho}}{2} \tag{2.13}$$

(5) Update $\boldsymbol{\mathcal{E}}$

$$\boldsymbol{\mathcal{E}} = arg\min\ \|\boldsymbol{\mathcal{E}}\|_1 + \frac{\rho}{2}\|\boldsymbol{\mathcal{D}} - \boldsymbol{\mathcal{L}} \times_1 \boldsymbol{U}^{(1)} \times_2 \boldsymbol{U}^{(2)} \times_3 \boldsymbol{U}^{(3)} - \boldsymbol{\mathcal{E}} + \frac{\boldsymbol{\lambda_1}}{\rho}\|^2 \tag{2.14}$$

Similar with $\boldsymbol{\mathcal{W}}$ by Soft-Thresholding under proxiaml operator:

$$\boldsymbol{\mathcal{E}} = S_{\frac{1}{\rho}}(\boldsymbol{\mathcal{D}} - \boldsymbol{\mathcal{L}} \times_1 \boldsymbol{U}^{(1)} \times_2 \boldsymbol{U}^{(2)} \times_3 \boldsymbol{U}^{(3)} + \frac{\boldsymbol{\lambda_1}}{\rho}) \tag{2.15}$$

(6) Update Lagrange multipliers $\boldsymbol{\lambda}_1, \boldsymbol{\lambda}_2$

$$\begin{aligned} \boldsymbol{\lambda}_1 &= \boldsymbol{\lambda}_1 + \rho(\boldsymbol{\mathcal{D}} - \boldsymbol{\mathcal{L}} \times_1 \boldsymbol{U}^{(1)} \times_2 \boldsymbol{U}^{(2)} \times_3 \boldsymbol{U}^{(3)} - \boldsymbol{\mathcal{E}}) \\ \boldsymbol{\lambda}_2 &= \boldsymbol{\lambda}_2 + \rho(\boldsymbol{\mathcal{L}} - \boldsymbol{\mathcal{G}} - \boldsymbol{\mathcal{W}}) \end{aligned} \tag{2.16}$$

Summarize all the above AL-ADM optimization processes to get the Algorithm2.

3. Experimental

(a) Experimental Set-up

The experimental schematic diagram of the proposed thermal imaging diagnostic system is shown in Fig. 1, Fig. 2 shows the corresponding real-time practical experimental equipment and facilities. An Easyheat 224 from Cheltenham Induction Heating is used for coil excitation. The Easyheat has a maximum excitation power of 2.4 kW, a maximum current of 400 Arms and an excitation frequency range of 150-400 kHz (380 Arms and 256 kHz are used in this study). Water cooling of the coil is implemented to counteract. direct heating of the coil. We use the IR camera (FLIR A655sc) and the frame rate is set to 100FPS to capture the thermal video sequences $D^{W \times H \times T}$, which have two kind of resolution :$W \times H$=120 $\times$ 640 and $W \times H = 240 \times 640$. The excitation signal generated by the excitation module is a small period of high frequency current. The current in the coil will induce the eddy currents and generate the resistive heat in the

Algorithm 2 Hierarchical Low R0ank and Sparse Tensor Decomposition(HLSTD) Algorithm

Input: Spatial-Temporal Thermalgraphy Tensor $\mathcal{D}^{W\times H\times T}$ rank r_1, r_2, r_3 .

1: Initialize: $\epsilon = 1e-5, \rho_0 = 1e-4, \rho_{max} = 1e10, \eta = 1.5, \boldsymbol{U}_0{}^{(i)} = \mathcal{L}_0 = \mathcal{G}_0 = \mathcal{W}_0 = \mathcal{E}_0$.
2: **while** not convergence **do**
3: Update $\boldsymbol{U}^{(i)}$ by (6) and (7) ;
4: Update $\mathcal{G}$ by (9) ;
5: Update $\mathcal{W}$ by (11) ;
6: Update $\mathcal{L}$ by (13) ;
7: Update $\mathcal{E}$ by (15) ;
8: Update $\boldsymbol{\lambda}_1$ and $\boldsymbol{\lambda}_2$ by (16) ;
9: Update $\rho = \min(\rho_{max}, \eta\rho)$;
10: Check the convergence conditions: $\|\mathcal{E}^{(k+1)} - \mathcal{E}^{(k)}\|_\infty < \epsilon$, $\|\mathcal{W}^{(k+1)} - \mathcal{W}^{(k)}\|_\infty < \epsilon$, $\|\mathcal{G}^{(k+1)} - \mathcal{G}^{(k)}\|_\infty < \epsilon$,$\|\mathcal{L} - \mathcal{G} - \mathcal{W}\|_\infty < \epsilon$ and $\|\mathcal{D}^{(k+1)} - \mathcal{L} \times_1 \boldsymbol{U}^{(1)} \times_2 \boldsymbol{U}^{(2)} \times_3 \boldsymbol{U}^{(3)} - \mathcal{E}^{(k+1)}\|_\infty < \epsilon$
11: **end while**

Output: Defect Tensor $\mathcal{G} \times_1 \boldsymbol{U}^{(1)} \times_2 \boldsymbol{U}^{(2)} \times_3 \boldsymbol{U}^{(3)} + \mathcal{E}$.

conductive material. The heat will diffuse in time until the heat reaches equilibrium in the material. Eddy current forced to divert due to meeting abnormal gullies at the defects, which lead to areas of increased and decreased eddy current density. Therefore, in the heating phase, different areas have different heat generation rates which subsequently lead to temperature spatial-transient variation.

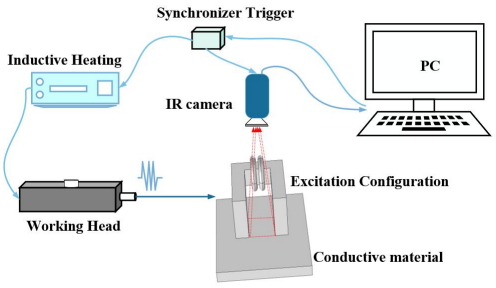

Figure 1: Inductive Thermography schematic diagram

(b) Defective Specimens

In order to illustrate the challenges faced by existing machine learning algorithms applied in Inductive Thermography Nondestructive Testing, we test them against the specimens which contain defects of irregular shapes. Specific test specimens are shown in Fig. 3. In particular, the complex characteristic of the rough surface of the specimens can be observed objectively but the micro cracks are invisible to the naked eye which leads to enormous difficulty in defect detection.

(c) Algorithm Evaluation Criteria

In order to validate the detection effectiveness of the proposed algorithm, we use the total computation time (as measured by the CPU) and signal-to-noise ratio (SNR) value as the numerical evaluation criteria. The SNR can evaluate the thermal contrast ratio between the

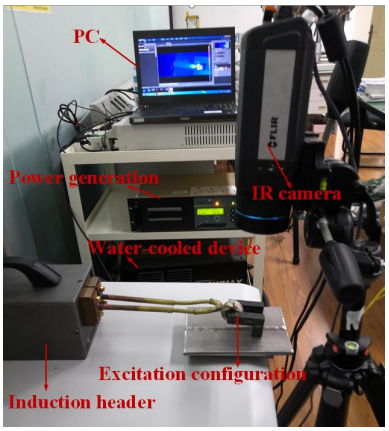

Figure 2: practical IT eperimental platform system

defective and non-defective regions as calculated according to $SNR = 20lg(\frac{T_d}{T_{non}})$, where T_d is the temperature of all pixels in the local thermal image 1-1 in Fig.5, Tnon is the temperature of all pixels in the local thermal image 1-2 within valid heating area near the defect. The size of area 1-2 is the same as area 1-1. The SNR of the entire thermal image is the average of the SNR calculated for all cracks. From the definition of SNR criteria, we can conclude intuitively that the more obvious the contrast between the defect and the surrounding of non-defect, the higher the SNR value. In other words, the higher the SNR value, the better the algorithm performance.

4. Results Analysis

Since the paper focuses on the important application of back-end processing algorithm in IT NDT, we select Tucker Decomposition [27], GMRTF [28], BRTF [19], TRPCA [17] for comparative verification, which are the latest algorithms in foreground background separation and sparse anomaly pattern detection. Subsequent experiments show that our algorithm can obtain more ideal and efficient results than other algorithms in Induction Thermography Detection System. In order to conduct fair comparison of running time, all images recovery experiments run in same platform, with Matlab 2018a under windows10 on a PC of a 3.30GHz i7-4590CPU and 16G RAM. The experimental parameters of each comparison algorithm either follow the default recommended settings in the paper or we adjust it to let perform well in most case. Visual results are listed in the Fig.6, SNR values and total CPU running time are shown Table 1.

(a) Comparison

In order to illustrate the difficulty and challenge of our special defect task detection in the field of nondestructive testing, we first show the processing results of the traditional feature extraction algorithm PCA [42], SPCA[43], the latest online sparse matrix algorithm SGSM-BS[35] and incremental tensor decomposition IMTSL [40] algorithm in Fig.4. More detailed experimental results are shown in supplementary materials. As observed from the above results, not only classical methods PCA and SPCA but also IMTSL ,SGSB-BS, fail in the specific detection task as shown in Fig.3 (a),(b),(c),(d). On the other hand, the proposed method has successfully detected the defects accurately where the defects' positions have been marked within the red boxes. In terms of energy concentration capabilities, the resulting images of the proposed algorithm show that the defects region (annotated with red boxes) are most centrally identified. According to the property of infrared thermography, the brighter the pixel, the higher the temperature which shows that these positions gather more energy. According to our SNR formula in paper:

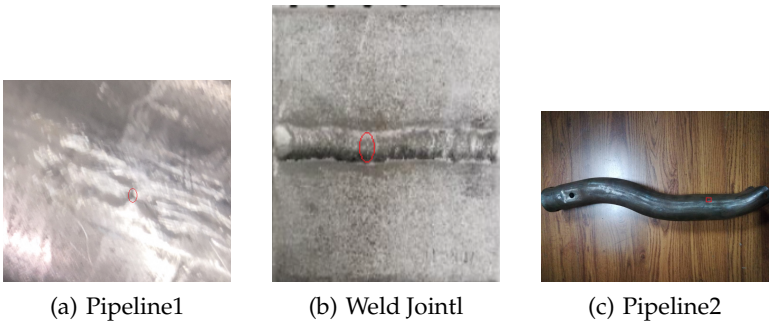

(a) Pipeline1 (b) Weld Jointl (c) Pipeline2

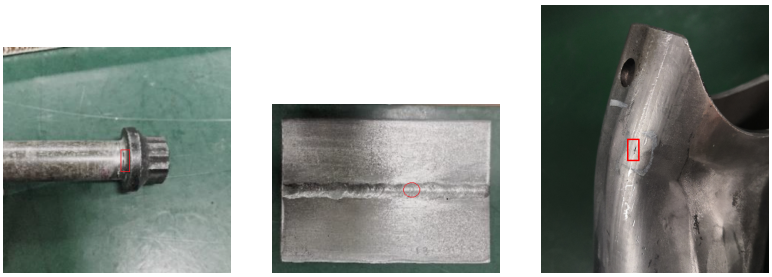

(d) Axel (e) Weld Joint2 (f) Low-Carbon Steel

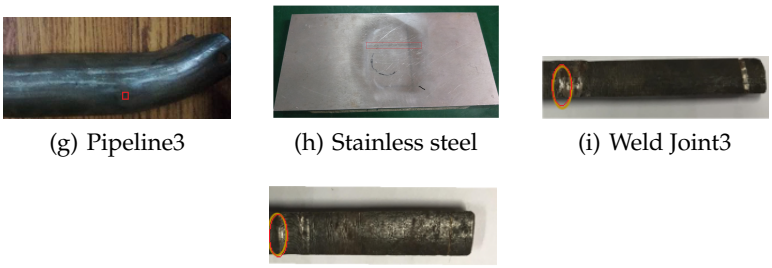

(g) Pipeline3 (h) Stainless steel (i) Weld Joint3

(j) Weld Joint4

Figure 3: Defective Specimen Objects Corresponding to Fig.6

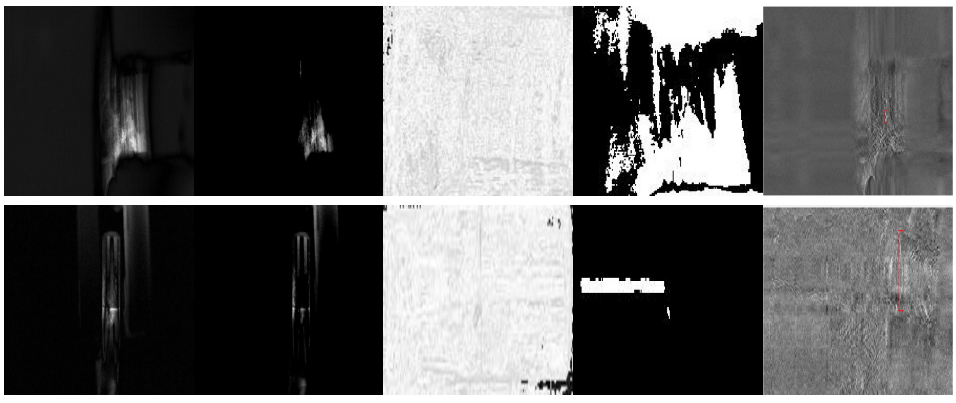

(a) PCA (b) SPCA (c) IMTSL (d) SGSM-BS (e) Proposed

Figure 4: Comparsion results (a)PCA. (b)SPCA. (c)IMTSL. (d)SGSM-BS. (e) Proposed

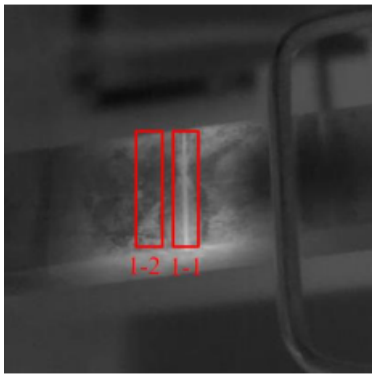

Figure 5: Illustration of SNR

$SNR = 20lg(T_d/T_{non})$, where T_d is the temperature of all pixels in the local thermal image 1-1 in Fig.5, T_{non} is the temperature of all pixels in the local thermal image 1-2 within valid heating area near the defect. Combined with description of energy concentration above, it can be observed that the proposed algorithm obtains higher T_d value and lower T_non value than other algorithms. In other words, the proposed method achieves higher SNR from the visual image results. Both the proposed algorithm and IMTSL(IHOSVD) are able to retain the details of the background of the test specimens. However, comparing with the IMTSL, the proposed algorithm could detect the defects with considerably higher signal-to-noise (SNR) and improved visual inspection. In addition, the IMTSL is very time-consuming, which cannot be tolerated in practical industrial applications as measured by the "run time" which is provided in Supplementary Materials.

It is worth mentioning that various advanced pulse compression favorable non-periodic thermal excitation techniques are in use for improving sub-surface defect detection and resolution in the field of infrared thermal wave imaging which also makes full use of heat map post-processing algorithms to detect defects. In addition, there are different forms of excitation schemes

Table 1: Comparative results SNR (Left) and total running time (Right in seconds)in Fig.3

Video Name	GMRTF		TUCKER		BRTF		TRPCA		Proposed	
	PSNR	Time	PSNR	Time	PSNR	Time	PSNR	Time	PSNR	Time
Sample1	-1.4	387.1	3.5	7.8	1.8	208.3	9.6	601.3	**12.9**	**5.1**
Sample2	0.8	128.1	1.9	3.8	1.4	105.9	0.8	227.5	**2.3**	**2.7**
Sample3	-14.6	528.9	2.1	8.6	-6.4	205.2	-1.2	597.7	**4.8**	**5.2**
Sample4	2.4	207.3	-1.7	7.0	-2.1	158.7	-1.2	449.6	**11.7**	**4.1**
Sample5	6.1	127.9	5.3	3.7	6.5	98.2	8.0	220.1	**12.6**	**3.5**
Sample6	8.3	466.7	-11.5	8.3	-13.1	204.2	-11.5	608.6	**9.4**	**5.1**
Sample7	5.4	355.1	5.1	8.4	2.3	209.7	1.6	601.1	**6.4**	**5.0**
Sample8	2.9	191.6	3.5	5.7	2.7	147.5	2.9	418.4	**4.2**	**3.8**
Sample9	1.4	361.2	-9.0	7.3	-12.8	210.3	1.9	609.6	**7.1**	**5.2**
Sample10	2.0	453.0	2.2	10.1	-1.3	209.0	8.5	614.1	**13.4**	**5.4**

(a) GMRTF (b) TUCKER (c) BRTF (d) TRPCA (e) Proposed

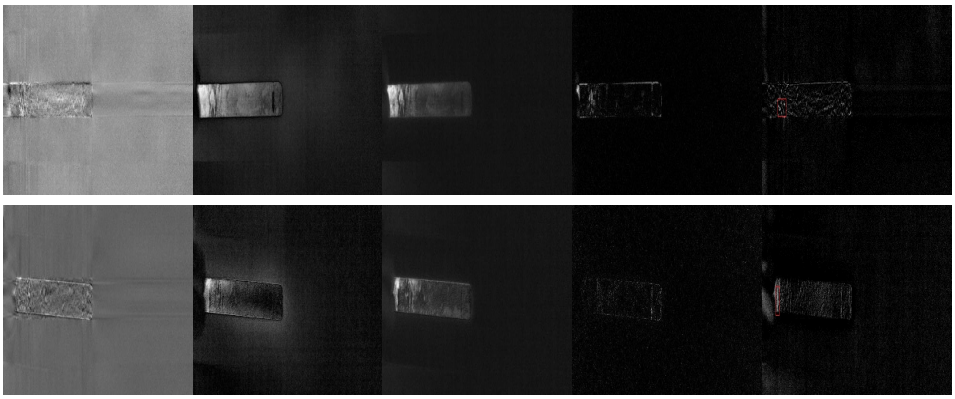

(f) GMRTF (g) TUCKER (h) BRTF (i) TRPCA (j) Proposed

Figure 6: Contrast of image visual effect in defect detection for IT.(Zoom in for better visual effect)

such as eddy current, ultrasound, laser excited thermographic techniques. More specifically, Ghali et. [44] proposed comparative data processing approaches for thermal wave imaging techniques for non-destructive testing. Siddiqui et. al proposed the Finite element analysis method for modelling the frequency modulated thermal wave imaging process in non-destructive testing of a mild steel sample [45]. Kaur et.al [46] proposed Principal Component Analysis (PCA) and Sparse PCA(SPCA) based post-processing schemes for improving spatial contrast over the defective regions and enhancing the signal to noise ratio (SNR) , which was applied in frequency modulated thermal wave imaging for inspection of steel material. In addition, Independent Component Analysis(ICA) was applied by Ahmad et. al on cross correlation data that improved the detectability, visibility, and contrast (in terms of signal-to-noise values) of the defects in Barker coded thermal wave imaging [47] and for frequency modulated thermal wave imaging [48], respectively. Albeit, as shown in Fig.4 (a) (b), traditional methods such as PCA ,SPCA and ICA perform inadequately in defect detection especially with moving test specimens. In contrast, the proposed algorithm yields considerable improvement over the traditional methods and has demonstrated high accuracy of defect detection using ECPT under the effect of moving speed. This is shown in Fig. 4 and Fig. 6 using samples 9 and sample 10, respectively.

From Fig.6 and Table 1, it is not difficult to judge whether in visual effect, SNR or running time value. The proposed algorithm shows the best performance among all methods. For GMRTF method, it assumes that the detection videos are corrupted by noise with unknown distribution, which they integrated the low rank tensor decomposition with mixture of Gaussian noise. To some extent, this is in line with the characteristics of IT data with strong noise and does not match with certain statistical law. From experiment results, it could eliminate high heat energy and strong noise to enhance defects. However, in the test of sample 1, sample 3 , sample 4, sample 6, the results of background heat elimination of GMRTF can not be compared with the performance of the proposed algorithm. The SNR values are -1.411 and -14.588 for sample 1 sample 3, respectively. Negative SNR means heat energy of non-defect higher than defect region in which may cause human to mistakenly recognize the high heat non-defect as defect from the image visual. On the other hand, these optimization are based on EM algorithm, which are utilized to update parameter under the framework of probability. This lead to GMRTF is not efficient compared with the proposed method. This prevents the application of this algorithm in large-scale real-time industrial detection.

With regard to Tucker decomposition, it only uses low rank decomposition, it cannot get rid of the strong thermal background of the defect. It is difficult to distinguish the defects with the

naked eye from the visual results. At the same time, it failed to enhance the contrast effect of defects. Albeit Tucker runs in a short time, saves 1-2 seconds in the experimental data set. In addition, the visual results of BRTF are similar with Tucker decomposition. But more importantly, the parameters are updated under full Bayesian inference framework, with the expansion of real data capacity as it is not scalable.

For Tucker and BRTF visual results under sparse decomposition, because sparse defections are still embedded in high thermal background. However, for TRPCA, it usually gets over-sparse results. From visuals of sample 1, 2, 3, 6, 9, 10, there exist too rare pixels to judge they are defects or not as it lacks of sufficient background information from specimens. What's worse, the algorithm requires a lot of matrix SVD operations, which consumes a lot of memory and computing resources and makes the speed of processing super slow.

In terms of robustness, although the comparison algorithm can detect defects on parts of specimens. For natural weld crack, this is corresponding test samples from 8-10. Natural weld crack is a great challenging task in practical inspection, because uneven surface is full of bumps and holes, as well as the extremely irregular shape. In 9-10 samples, all of comparison algorithms fail to detect the weld crack, where the proposed HLSTD get the detection with high resolution and obvious enhancement. In terms of running time, the proposed algorithm gets the fastest speed with average 4.5 seconds.

(b) Robustness of the proposed HLSTD

The robustness of the proposed HLSTD algorithm is measured as the effectiveness of hierarchical decomposition for defect detection in the presence of complex background and strong noise. Specifically, defect information may be extracted in $\boldsymbol{\mathcal{E}}$ of the first layer or in $\boldsymbol{\mathcal{G}} \times_1 \boldsymbol{U}^{(1)} \times_2 \boldsymbol{U}^{(2)} \times_3 \boldsymbol{U}^{(3)}$ of the second layer. Albeit the algorithm cannot predict in advance which part of the two components the defect will fall into. We integrate two parts to ensure that the defect can be extracted accurately and effectively, and the interference of noise and high-energy background is discarded. By relying only on a certain individual component, there is no guarantee that the algorithm can accurately extract the target defects. Hence the need for the proposed algorithm to incorporate the hierarchical nature of the decomposition in order to obtain robust defects detection. The following comparison of the intermediate experimental results shows the robustness of the HLSTD algorithm. For the sake of brevity, we mark $\boldsymbol{\mathcal{E}}$ and $\boldsymbol{\mathcal{G}} \times_1 \boldsymbol{U}^{(1)} \times_2 \boldsymbol{U}^{(2)} \times_3 \boldsymbol{U}^{(3)}$ with $\boldsymbol{\mathcal{C}}_1$ and $\boldsymbol{\mathcal{C}}_2$ respectively. In Fig.7, images from top to bottom correspond to the corresponding to the first five test pieces in Fig.6, respectively.

Rank r1, r2, r3 are all set as 20, 20, 10 and $\lambda = \frac{1}{\sqrt{r_3 \max(r_1, r_2)}}$ for all specimens in the proposed method. Albeit defects lie in different component $\boldsymbol{\mathcal{C}}_i$ for different specimens, i=1, 2. It is observed that the first two defects lie in $\boldsymbol{\mathcal{C}}_1$, and the last three lie in $\boldsymbol{\mathcal{C}}_1$. The first two defects can't be judged by combining the background information well because the image only contains the bright spot information in the state of over sparse. Because of the low rank representation, the image showing the defect in $\boldsymbol{\mathcal{C}}_2$ component does not retain the background information well and hence it resulted in blurred visual effect. The integration of $\boldsymbol{\mathcal{C}}_1$ and $\boldsymbol{\mathcal{C}}_2$ not only robustly extracts the defect with the background information preserved, but also produces a clearer visual results.

5. Conclusion

In this paper, we have proposed a novel Hierarchal Low Rank and Sparse Tensor Decomposition (HLSTD) algorithm. We have also developed it for Inductive Thermography for nondestructive defects detection. Natural crack defects in a variety of specimens with irregular shape have been used and validated by different advanced unsupervised decomposition methods and subsequently compared with the proposed algorithm. The proposed algorithm can accurately and efficiently suppress high heat background and strong noise while separating and enhancing the visual defects embedded in the thermal video stream. Both visual effects and numerical results have verified that the robustness and efficiency of the proposed for defects detection.

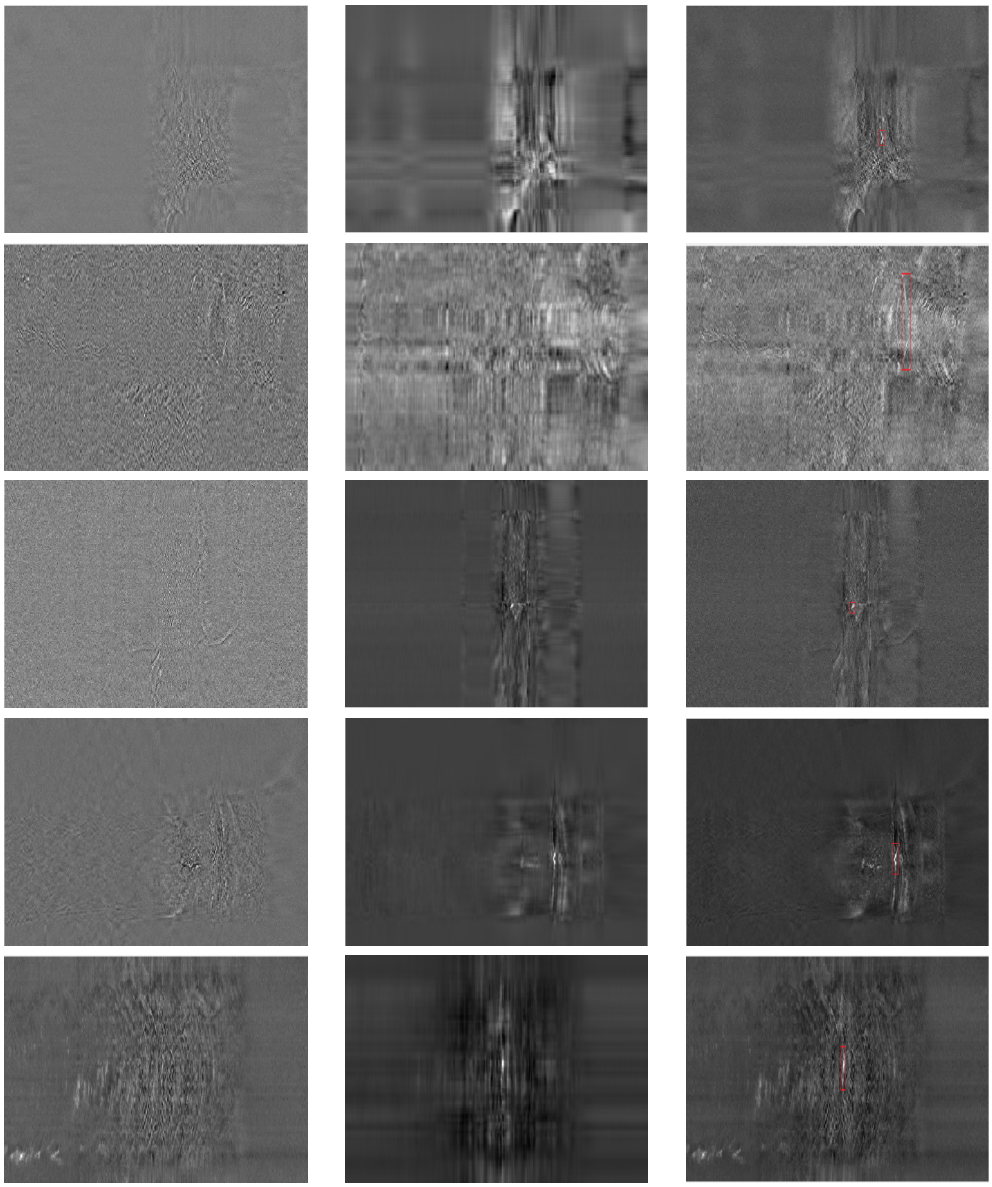

(a) $\mathcal{C}_1$ (b) $\mathcal{C}_2$ (c) $\mathcal{C}_1$+$\mathcal{C}_2$

Figure 7: Robustness of HLSTD

Acknowledgements. The work was supported by National Natural Science Foundation of China (No. 61971093, No. 61527803, No. 61960206010). The work was supported by Science and Technology Department of Sichuan, China (Grant No.2019YJ0208, Grant No.2018JY0655, Grant No. 2018GZ0047) and Fundamental Research Funds for the Central Universities (Grant No. ZYGX2019J067).

References

1. Goumeidane, Khamadja, and Odet. Parametric active contour for boundary estimation of weld defects in radiographic testing, in *International Symposium on Signal Processing Its Applications*,

2007.
2. D. rer. nat. Dr.-Ing. E. h. Josef KrautkrAmer. Ultrasonic testing of Ëmaterials, 1977.
3. P. E. Mix. Magnetic Particle Testing, 2005.
4. L. Huang, M. O. Xia-Lin, L. J. Zhu, and S. M. Yang. Liquid penetrate testing of tiny defects, Nondestructive Testing, 2013.
5. B. Gao, W. L. Woo, Y. He, and G.Y. Tian. Unsupervised sparse pattern diagnostic of defects with inductive thermography imaging system, *IEEE Transactions on Industrial Informatics, vol. 12, no. 1, pp. 371-383*, 2016.
6. B. Gao, L. Bai, G.Y. Tian, W. L. Woo, and Y. Cheng. Spatial and time patterns extraction of eddy current pulsed thermography using blind source separation, *IEEE Sensors Journal, vol. 13, no. 6, pp. 2094-2101*, 2013.
7. L. Cheng, B. Gao, G.Y. Tian, W. L. Woo, and G. Berthiau. Impact damage detection and identification using eddy current pulsed thermography through integration of PCA and ICA, *IEEE Sensors Journal, vol. 14, no. 5, pp. 1655-1663*, 2014.
8. M. Genest, D. C. Dudzinski, L. Dawag, and R. K. Kersey. Crack detection using induction thermography during high temperature testing, in *Spie Defense, Security, Sensing*, 2013.
9. P. JAckel and U. Netzelmann. The influence of external magnetic fields Ë on crack contrast in magnetic steel detected by induction thermography, *Quantitative Infrared Thermography Journal, vol. 10, no. 2, pp. 237-247*, 2013.
10. Y. He, G.Y. Tian, M. Pan, D. Chen, and Z. Hong. An investigation into eddy current pulsed thermography for detection of corrosion blister, *Corrosion Science, vol. 78, no. 1, pp. 1-6*, 2014.
11. N. Han, Y. Song, and Z. Song. Bayesian robust principal component analysis with structured sparse component, *Computational Statistics Data Analysis, vol. 109, pp. 144-158*, 2017.
12. P. Netrapalli, U. N. Niranjan, S. Sanghavi, A. Anandkumar, and P. Jain. Non-convex robust PCA, *Computer Science, pp. 1107-1115*, 2017.
13. B. Lois and N. Vaswani. Online matrix completion and online robust PCA, 2015.
14. B. Gao, W. Woo, and S. Dlay. Variational regularized 2-d nonnegative matrix factorization, *IEEE Transactions on Neural Networks Learning Systems, vol. 23, no. 5, pp. 703-716.*
15. B. Gao, L. Peng, W. L. Woo, G.Y. Tian, and M. Johnston. Variational Bayesian sub-group adaptive sparse component extraction for diagnostic imaging system, *IEEE Transactions on Industrial Electronics, vol. 65, no. 10, pp. 8142-8152*, 2018.
16. Y. Wang, B. Gao, W. L. Woo, G.Y. Tian, and Y. Zhu. Thermal pattern contrast diagnostic of micro cracks with induction thermography for aircraft braking components, *IEEE Transactions on Industrial Informatics, vol. PP, no. 99, pp. 1-1*, 2018.
17. C. Lu, J. Feng, Y. Chen, W. Liu, Z. Lin, and S. Yan. Tensor robust principal component analysis with a new tensor nuclear norm. *IEEE Transactions on Pattern Analysis and Machine Intelligence*, 2018.
18. R. Zdunek. Nonnegative matrix and tensor factorizations, 2009.
19. Q. Zhao, G. Zhou, L. Zhang, A. Cichocki, and S. Amari. Bayesian robust tensor factorization for incomplete multiway data, *IEEE Transactions on Neural Networks Learning Systems, vol. 27, no. 4, pp. 736-748*, 2017.
20. Z. Pan and J. Feng. Outlier-robust tensor PCA, in *IEEE Conference on Computer Vision Pattern Recognition*, 2017.
21. B. Gao, A. Yin, Y. Wang, G.Y. Tian, W. L. Woo, and H. Liu. Thermography spatial-transient-stage tensor model and materal property characterization, in *Nondestructive Evaluation/testing*, 2014.
22. B. Gao, Y. He, W. Lok Woo, G.Y. Tian, J. Liu, and Y. Hu. Multidimensional tensor-based inductive thermography with multiple physical fields for offshore wind turbine gear inspection, *IEEE Transactions on Industrial Electronics, vol. 63, no. 10, pp. 6305-6315*.
23. L. Peng, B. Gao, Q. Feng, Y. Yang, and G.Y. Tian. Ensemble variational Bayes tensor factorization for super resolution of cfrp debond detection, *Infrared Physics Technology, vol. 85, p. 335-346, 2017*.
24. C. Zhang, H. Fu, L. Si, G. Liu, and X. Cao. Low-rank tensor constrained multiview subspace clustering, in *IEEE International Conference on Computer Vision*, 2015.
25. W. Hu, D. Tao, W. Zhang, Y. Xie, and Y. Yang. The twist tensor nuclear norm for video completion, *IEEE Transactions on Neural Networks Learning Systems, vol. 28, no. 12, pp. 2961-2973*, 2017.
26. J. C. Gower and G. B. Dijksterhuis. Orthogonal Procrustes problems, 2004.

27. T. G. Kolda and B. W. Bader. Tensor decompositions and applications, *Siam Review, vol. 51, no. 3, pp. 455-500*, 2009.
28. X. Chen, H. Zhi, W. Yao, Z. Qian, D. Meng, L. Lin, and Y. Tang. A general model for robust tensor factorization with unknown noise. 2017.
29. E. Candes, X. Li, Y. Ma, J. Wright, âRobust Principal Component Analysisâ, *ACM, Volume 58, No. 3, May 2011*.
30. Namrata Vaswani, Thierry Bouwmans, Sajid Javed, Praneeth Narayanamurthy: Robust Subspace Learning: Robust PCA, Robust Subspace Tracking, and Robust Subspace Recovery. *IEEE Signal Process. Mag. 35(4): 32-55 (2018)*
31. Vaswani N , Chi Y , Bouwmans T . Rethinking PCA for Modern Data Sets: Theory, Algorithms, and Applications [Scanning the Issue][J]. *Proceedings of the IEEE, 2018, 106(8):1274-1276*.
32. Bouwmans, T. , Sobral, A. , Javed, S. , Jung, S. K. , Zahzah, E. H. . (2017). Decomposition into low-rank plus additive matrices for background/foreground separation: a review for a comparative evaluation with a large-scale dataset. Computer ence review, 23(Feb.), 1-71.
33. Q. Gu, Z. Wang, H. Liu, âLow-Rank and Sparse Structure Pursuit via Alternating Minimizationâ, International Conference on Artificial Intelligence and Statistics, AISTATS 2016, May 2016.
34. M. Ma, R. Hu, S. Chen, J. Xiao, Z. Wang, âRobust Background Subtraction Method via Low-Rank and Structured Sparse Decomposition , *Networks and Security, pages 156-167, July 2018*.
35. Guangming, S. , Tao, H. , Weisheng, D. , Jinjian, W. , Xuemei, X. . (2018). Robust foreground estimation via structured gaussian scale mixture modeling. IEEE Transactions on Image Processing, 1-1.
36. Sajid Javed, Arif Mahmood, Somaya Al-MÃ¡adeed, Thierry Bouwmans, Soon Ki Jung: Moving Object Detection in Complex Scene Using Spatiotemporal Structured-Sparse RPCA. *IEEE Trans. Image Processing 28(2): 1007-1022 (2019)*
37. J. Xue, Y. Zhao, W. Liao, J. Chan, âNonconvex tensor rank minimization and its applications to tensor recoveryâ, *Information Sciences, Volume 503, pages 109-128, 2019.*
38. W. Chen, X. Gong, N. Song, "Nonconvex Robust Low-Rank Tensor Reconstruction via an Empirical Bayes Methodsâ, *IEEE Transactions on Signal Processing, Volume 67, No. 22, pages 5785-5797, 2019.*
39. Sajid Javed, Thierry Bouwmans, Soon Ki Jung:Stochastic decomposition into low rank and sparse tensor for robust background subtraction. ICDP 2015: 1-6
40. Andrews Sobral, Christopher G. Baker, Thierry Bouwmans, El-hadi Zahzah: Incremental and Multi-feature Tensor Subspace Learning Applied for Background Modeling and Subtraction. ICIAR (1) 2014: 94-103
41. C. Qiu, X. Wu, H. Xu, "Recursive Projected Sparse Matrix Recovery (ReProCSMR) With Application In Real-Time Video Layer Separation", ICIP 2014, pages 1332-1336, October 2014.
42. Jolliffe, I. T. Principal Component Analysis. *2nd ed., Springer, 2002.*
43. T. Cai, Z. Ma, Y. Wu: Recent results on sparse principle component analysis. CAMSAP 2013: 181-183
44. Ghali V S , Mulaveesala R . Comparative Data Processing Approaches for Thermal Wave Imaging Techniques for Non-Destructive Testing[J]. Sensing Imaging An International Journal, 2011, 12(1-2):15-33.
45. J A Siddiqui, V Arora, R Mulaveesala, A Muniyappa. (2015). Modelling of the frequency modulated thermal wave imaging process through the finite element method for non-destructive testing of a mild steel sample. Insight Non Destructive Testing Condition Monitoring, 57(5), 266-268(3).
46. Kaur, K., Mulaveesala, R. An efficient data processing approach for frequency modulated thermal wave imaging for inspection of steel material (2019) Infrared Physics and Technology, 103, art. no. 103083, .
47. Ahmad, J., Akula, A., Mulaveesala, R., Sardana, H.K.Defect detection capabilities of independent component analysis for Barker coded thermal wave imaging (2020) Infrared Physics and Technology, 104, art. no. 103118, .
48. Ahmad, J., Akula, A., Mulaveesala, R., Sardana, H.K. An independent component analysis based approach for frequency modulated thermal wave imaging for subsurface defect detection in steel sample (2019) Infrared Physics and Technology, 98, pp. 45-54.